




Properties of (Fe–B)-doped Sn–1.0Ag–0.5Cu solders prepared by mechanical alloying

Ruo-Da Wang, Qiang Hu* , Shao-Ming Zhang, Fu-Wen Zhang, Cai-Tao Lu, Zhi-Gang Wang

Received: 25 September 2018 / Revised: 26 November 2018 / Accepted: 14 March 2019 / Published online: 8 April 2019
© The Nonferrous Metals Society of China and Springer-Verlag GmbH Germany, part of Springer Nature 2019

Abstract To introduce boron (B) into the Sn–1.0Ag–0.5Cu (SAC105) solder, based on the thermodynamic calculations, iron (Fe) is a competent carrier component for bonding B and Sn. The Sn–Fe–B master alloys were prepared by mechanical alloying initially; then, the SAC105-0.05(Fe–B) and SAC105-0.1(Fe–B) solder alloys were prepared using 72-h-milling Sn–Fe–B master alloys. The preparation process and the properties of solders were studied in this work. For the Sn–Fe–B master alloys, the results show that with the increase in the ball-milling time, the powder changes illustrate a cold welding–crushing–cold welding cyclic process. Moreover, the supersaturated solid solubility of (Fe–B) increases gradually in the alloys' matrix and the lattice distortion increases to 0.167% after 72-h milling. Meanwhile, the alloying degree is increasingly apparent, and after 72-h milling, the content of B in the Sn matrix reaches 2.38 wt%. For the solder alloys, with the (Fe–B) content increasing, the melting point decreases and a significant grain refinement occurs in the matrix. Compared to the benchmark SAC105, the hardness of SAC105-0.05(Fe–B) and SAC105-0.1(Fe–B) solder alloys prepared by this method is improved by 20.65% and 34.79%, respectively. The present research provides a novel approach for introducing the immiscible component into the lead-free solder alloys.

Keywords Sn–1.0Ag–0.5Cu; Sn–Fe–B; Mechanical alloying; Supersaturated solid solution

1 Introduction

With the development of lead-free electronic packaging and assemble materials, the researches of new lead-free solder that can replace the non-environmental friendly Sn–Pb solder have become the focus currently [1–3]. Also, the development of new Sn-based lead-free solder alloys emerges endlessly. At present, the Sn–Ag–Cu (SAC) alloy has been the most suitable lead-free solders because of its advantages in good performance and reliability [4]. However, there are still some imperfections in the SAC alloys. For example, the brittle intermetallic compounds (IMCs) in high-Ag-content solders in solder joints, i.e., Cu_6Sn_5 , Cu_3Sn , and coarsening Ag_3Sn , will seriously weaken the mechanical performance and reliability [5, 6]. Currently, the Sn–1.0Ag–0.5Cu (SAC105) low-silver lead-free solders have become the research hotspot for its significant benefit of reducing the cost and amount of coarsening Ag_3Sn phase [7]. Nevertheless, the mechanical properties of SAC105 solders were lower than those of Sn–3.0Ag–0.5Cu (SAC305) because of the decreased Ag content and the coarsening microstructure. It is considered that there is an actual requirement for novel high-performance SAC105 solders with the added solute to refine the microstructure, improving the mechanical properties and the reliability of solder alloys.

The present study shows that the amount of Fe particles can refine the microstructure of the solder, and the amount of Fe (0.05 wt%) can achieve better wettability of the solder alloy, while the tensile strength also gets a good performance [8]. The addition of B can influence the

R.-D. Wang, Q. Hu*
General Research Institute for Nonferrous Metals,
Beijing 100088, China
e-mail: hqgrinm@163.com

R.-D. Wang, Q. Hu, S.-M. Zhang, F.-W. Zhang, C.-T. Lu,
Z.-G. Wang
Beijing COMPO Advanced Technology Co., Ltd.,
Beijing 101407, China

morphology of IMC. Simultaneously, the vertical grain growth rates of brittle IMC can be slowed down [6, 9–11]. Therefore, Fe and B were introduced into Sn matrix to prepare the novel (Fe–B)-doped Sn–1.0Ag–0.5Cu alloys to improve the properties of solder alloys. However, B is difficult to introduce into Sn matrix, because B belongs to the immiscible substance. To tackle it, the Fe has been suggested as a carrier to introduce B into Sn matrix to fabricate Sn–Fe–B master alloys initially using mechanical alloying (MA) method. During the milling process, the particles get a strong plastic deformation, resulting in many defective particles. It can significantly reduce the material diffusion activation energy. So, the multiphase chemical reaction, which is difficult to carry out, can be induced by mechanical alloying under normal or low temperature [12–14]. Besides, previous studies indicated that the supersaturated solid solutions could occur in almost all alloy systems with high-energy ball milling [15]. This approach is not only optimized for obtaining Sn–Fe–B master alloys with uniform composition but also can improve the production efficiency [12]. Most notably, it is the first attempt to prepare Sn–Fe–B novel master alloys by mechanical alloying.

Furthermore, Fe is supposed more easily to form compounds and alloys with Sn and B, which can be considered as a bond of immiscible phases between Sn and B. To confirm this conjecture, the thermodynamics calculation based on Miedema model [16] can be used. Subsequently, by utilizing the synthesized Sn–Fe–B master alloys, SAC105-0.05(Fe–B) and SAC105-0.1(Fe–B) solders were prepared to examine its practicability. Also, the performance of the novel solder alloys was tested synchronously.

2 Experimental

2.1 Miedema model for thermodynamics calculation

On the basis of mechanical alloying of binary immiscible alloy systems, the metastable phase, i.e., supersaturated solid solution, amorphous, and nanocomposite, can be prepared, which shows the unique properties compared with alloy with microscale structure. The existing research shows that the thermodynamic calculation method developed by Miedema et al. [17] has been applied by the researchers to calculate thermodynamic of the mechanical alloying process of the binary insoluble alloy system. The Miedema model is an important theory for calculating the formation process of most binary alloy systems. The purpose of this work is to calculate the thermodynamic properties of boron–tin (B–Sn), boron–iron (B–Fe), and tin–iron (Sn–Fe) via Miedema model, to demonstrate its

feasibility and formation mechanism. The formula of activity coefficient calculated is given by Refs. [17–19].

For the binary alloy systems, the dissolution heat of component A dissolved in component B ($H_{\text{sol}}^{\text{AinB}}$) can be calculated as the following formula:

$$H_{\text{sol}}^{\text{AinB}} = \frac{2(V_{\text{A}}^{2/3})_{\text{alloy}} \left\{ -(\phi_{\text{A}}^* - \phi_{\text{B}}^*)^2 P + [(n_{\text{ws}}^{\text{A}})^{-1/3} - (n_{\text{ws}}^{\text{B}})^{-1/3}]^2 Q - \alpha R \right\}}{(n_{\text{ws}}^{\text{A}})^{-1/3} + (n_{\text{ws}}^{\text{B}})^{-1/3}} \quad (1)$$

The enthalpy of formation for a binary alloy system (ΔH_{c}) can be calculated by:

$$\Delta H_{\text{c}} = x_{\text{A}} f_{\text{B}}^{\text{A}} \Delta H_{\text{sol}}^{\text{AinB}} \quad (2)$$

In Eq.(1), the specific term can be calculated by:

$$(V_{\text{A}}^{2/3})_{\text{alloy}} = (V_{\text{A}}^{2/3})_{\text{pureA}} [1 + \beta f_{\text{B}}^{\text{A}} (\phi_{\text{A}}^* - \phi_{\text{B}}^*)] \quad (3)$$

$$f_{\text{B}}^{\text{A}} = C_{\text{B}}^{\text{S}} \left[1 + \gamma (C_{\text{A}}^{\text{S}} C_{\text{B}}^{\text{S}})^2 \right] \quad (4)$$

$$C_{\text{A}}^{\text{S}} = \frac{x_{\text{A}} V_{\text{A}}^{2/3}}{x_{\text{A}} V_{\text{A}}^{2/3} + x_{\text{B}} V_{\text{B}}^{2/3}} \quad (5)$$

$$C_{\text{B}}^{\text{S}} = \frac{x_{\text{B}} V_{\text{B}}^{2/3}}{x_{\text{A}} V_{\text{A}}^{2/3} + x_{\text{B}} V_{\text{B}}^{2/3}} \quad (6)$$

where x_{A} and x_{B} are the amounts of A and B components, $x_{\text{A}} + x_{\text{B}} = 1$; ϕ_{A}^* , ϕ_{B}^* are the electronegativities of A and B elements; n_{ws}^{A} and n_{ws}^{B} are the densities of electrons at the Wigner–Seitz cell boundary; V_{A} , V_{B} are the molar volumes of A and B components; C_{A}^{S} and C_{B}^{S} are the surface concentrations; f_{B}^{A} accounts for the concentration dependence; γ is the chemical short-range order parameter of binary alloy; P , Q , R , α , and β are the empiric constants determined by Miedema et al. [16], $Q/P = 9.4$, $\alpha = 0.73$ for liquid alloys, whereas $\alpha = 1$ for solid alloys, $\beta = 0.14$ for alkaline metals, whereas $\beta = 0.10$ for 2-valence metals, $\beta = 0.07$ for 3-valence metals, and 3.00 for silver, gold, and copper. In all other cases, $\beta = 0.04$. P relies on whether A and B are transition or non-transition metals; $P = 12.3$ when A is a transition metal and B is a non-transition metal; $P = 14.1$ when A and B are transition metals; $P = 10.6$ when A and B are non-transition metals; $R/P = 0$ when both A and B are transition or non-transition metals.

For the above formula, in particular, whose component is a semiconductor or a nonmetal, the enthalpies of transformation ($\Delta H_{\text{A}}^{\text{trans}}$ or $\Delta H_{\text{B}}^{\text{trans}}$) are also required. Hence, the final formula for binary alloy system can be determined as:

$$\Delta H = \Delta H_{\text{c}} + x_{\text{A}} \Delta H_{\text{A}}^{\text{trans}} + x_{\text{B}} \Delta H_{\text{B}}^{\text{trans}} \quad (7)$$

2.2 Materials

The Fe–B alloy powder and the pure Sn powder (particle size of 20–70 μm) were utilized as the raw materials. In the mechanical alloying process, to ensure better alloying effect, for refractory alloy elements, the appropriate adding amount is 8 wt%–10 wt% [20]. Thus, 10 wt% of the Fe–B alloy was selected to add into the solder alloys to achieve the good alloying effect. The inductively coupled plasma-atomic emission spectrometry (ICP-AES) was used to analyze the binary composition of Fe–B alloy under equilibrium state, and the B content is 19.65 wt%, therefore, the ratio of Fe to B is around 8:2. Combining with the phase diagram of Fe–B alloy, it is mainly composed of FeB (about 16 wt%) and the remainder is B particles.

The experimental materials are composed of pure Sn powder and Fe–B alloy powder. The mechanical alloying adopts the QM-1sp12-type planetary ball mill, and its rotation ratio (rotation: revolution) is 1.9:1, setting the rotation speed as $\omega_r = 200 \text{ r}\cdot\text{min}^{-1}$. The powder, according to the proportion of Sn-10% (Fe–B), was loaded into the 500-ml stainless-steel vacuum ball-milling tank after being mixed. The agate balls with the diameter of 3–8 mm were used as the milling ball. The ratio of the ball to powder material was set as 10:1, and the loading ratio was set at 50%. The alcohol was used as a wet-milling medium. The 2 wt% rosin was utilized as grinding aid material. The nitrogen was filled with the tank as protective gas. Then, the ball-milling tanks were loaded onto a ball mill to perform ball milling, milling 0, 24, 48, and 72 h, respectively. The slurries prepared were placed in DZF-6020 vacuum drying box to dry for 24 h after wet milling, and then, the samples were taken as the master alloys for the preparation of (Fe–B)-doped SAC105 lead-free solders.

The powder was mixed with Sn, Sn–20Ag, and Sn–10Cu, and then, the blended powder was melted in a ceramic crucible under the covering rosin at 300 °C to prepare the SAC105-0.05(Fe–B) and SAC105-0.1(Fe–B) solder alloys (wt%), in detail, SAC105-0.04Fe-0.01B and SAC105-0.08Fe-0.02B, after uniformly blending, and the alloy melt was cast into block mold.

2.3 Sample testing and characterization

The oxygen content of Sn–Fe–B alloy samples was analyzed by O-3000-type oxygen content analyzer. The ICP-AES analyzer was used to analyze the elements in the alloy matrix. The X-ray diffraction (XRD) phases were analyzed by the Japanese Science (RIGAKU) Smart-lab X-ray diffraction detector. The ZEISS-Axiovert 200MAT optical microscope (OM) was applied to the observation of microstructure in bulk samples. The morphology of the powders was observed by JEOL JSM-6510 scanning

electron microscope (SEM), and the energy-dispersive spectrometer (EDS) analysis was carried out to determine the constituents. The melting behaviors were measured by Netzsch differential scanning calorimeter (DSC) 409 PC differential scanning calorimeter, and the hardness of solder alloy ingots was tested by Leeb-140-type (HLD) hardness tester at room temperature.

3 Results and discussion

3.1 Sn–Fe–B master alloys

3.1.1 Enthalpy of formation for binary alloy system

The enthalpies of formation for B–Sn, B–Fe, and Fe–Sn binary alloy systems were calculated by the Miedema model. The curve diagrams that change with the composition content are shown in Fig. 1.

In general, the enthalpy of formation for B–Sn is positive ($\Delta H_{\text{sol}}^{\text{BinSn}} > 0$), which means that B and Sn are not appropriate to form the equilibrium-state binary alloys. Nevertheless, the possibility of formation of the supersaturated solid solution can be taken into consideration [20, 21]. Although the thermodynamic driving force for the formation of the supersaturated solid solutions is limited, the researchers believe that the formation of the supersaturated solid solution in the mechanical alloying process of the insoluble binary system depends on the dynamic conditions. To be more specific, the existence of crystal defects introduced by high-energy ball milling and the increase in the interface energy caused by the refinement of the microstructures to the nanometer scale can promote the expansion of the solid solubility of the insoluble system [21]. On the other hand, most of formation enthalpies for B–Fe and Fe–Sn are less than zero ($\Delta H_{\text{sol}}^{\text{BinFe}} < 0$, $\Delta H_{\text{sol}}^{\text{FeinSn}} < 0$), which indicates that the B–Fe and Fe–Sn can be synthesized as the alloys. From the perspective of introducing B into the Sn matrix, Fe can be considered as a competent component in this work.

3.1.2 Oxygen content analysis

The oxygen content analysis, shown in Table 1, indicates that with the milling time increasing, oxygen content shows a trend of a gradual rise (taking the experimental error into consideration). The appropriate oxygen can increase the solid solubility of the alloy. Yavari and Desré [22] considered that improving the solubility of oxygen in the alloy is because oxidation reaction leads to the formation of negative enthalpy of mixing compounds.

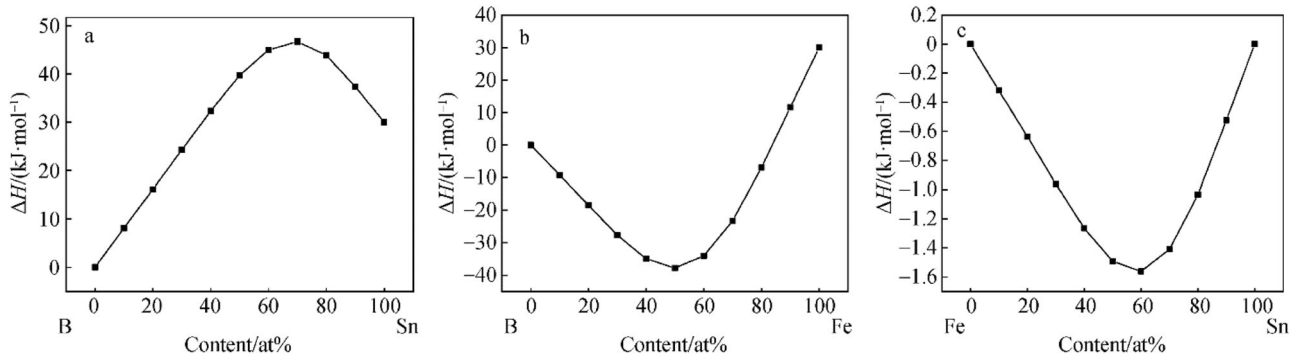


Fig. 1 Enthalpy of formation for binary alloy systems in this work: **a** B in Sn, **b** B in Fe, and **c** Fe in Sn

Table 1 Oxygen content values of powder samples with different ball-milling time

Alloy types	Sn	Sn–Fe–B			
Time/h	0	0	24	48	72
O ₂ content/ 10^{-6}	70.28	928.51	3919.88	3239.39	4154.00

3.1.3 Chemical composition analysis

The chemical analysis (ICP-AES) of the alloys' matrix is presented in Fig. 2. As can be seen, with the increase in ball-milling time, the content of B shows a tendency of gradual increase, indicating that with the rise of ball-milling time, the B has been introduced into the Sn matrix continuously.

3.1.4 Phase analysis

To illustrate the evolution of phases' rule and the alloying degree, the crystal structures and phase transformation of Sn were investigated by XRD and Rietveld powder diffraction profile-fitting technique. XRD patterns of Sn–

Fe–B (marked as SFB in the diagram) alloys are presented in Fig. 3. As indicated, combining with the XRD patterns, the results of the phase analysis JCPDS card Nos. are listed in Table 2.

According to Fig. 3 and phase analysis, after powder blending, the diffraction peaks of Sn and FeB are obvious. After 24-h ball milling, XRD peak for FeB phase has almost disappeared, and no new phases generate. Simultaneously, the peak for the Sn phase position shifts a small angle, suggesting that partial supersaturated solid solution has occurred between FeB and Sn [23, 24]. After 72-h ball milling, the diffraction peak of FeB disappears completely, and the peak of the Sn phase position shifts larger than that after 24 h. Consequently, FeB has dissolved into Sn as the supersaturated solid solution completely.

The broadening and dwarfing of diffraction peak were caused by lattice distortion and grain refinement. The crystalline size can be calculated by the Scherrer equation [25]:

$$\beta = \frac{\zeta \lambda}{d_c \cos \theta} \quad (8)$$

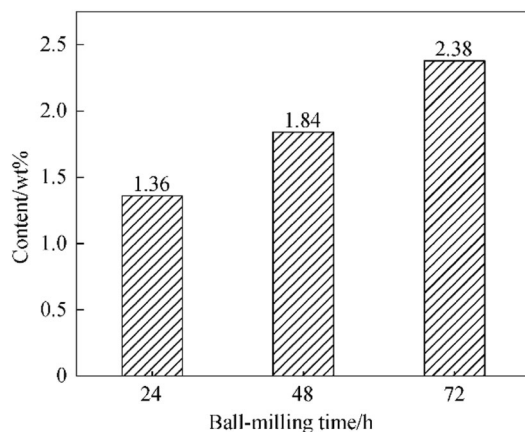


Fig. 2 Chemical analysis of B content by ICP-AES

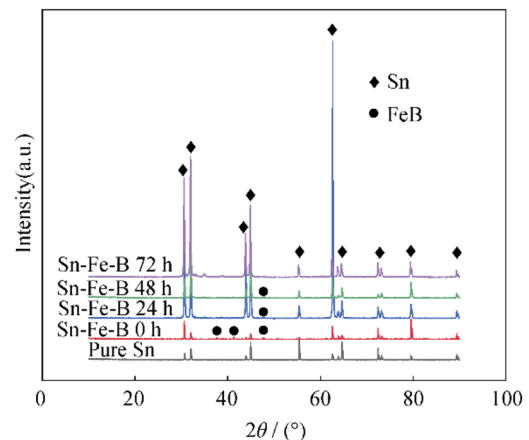


Fig. 3 XRD patterns of Sn–Fe–B alloys with different milling time

Table 2 Phase analysis JCPDS Nos. of Sn–Fe–B alloys in this study

Powder	Phase	Crystal structure	JCPDS Nos.
Non-milled	Sn	Body-centered tetragonal	04-0673
	FeB	–	76-0092
Milled for 24, 48, and 72 h	Sn	Body-centered tetragonal	04-0673
	FeB	–	32-0483

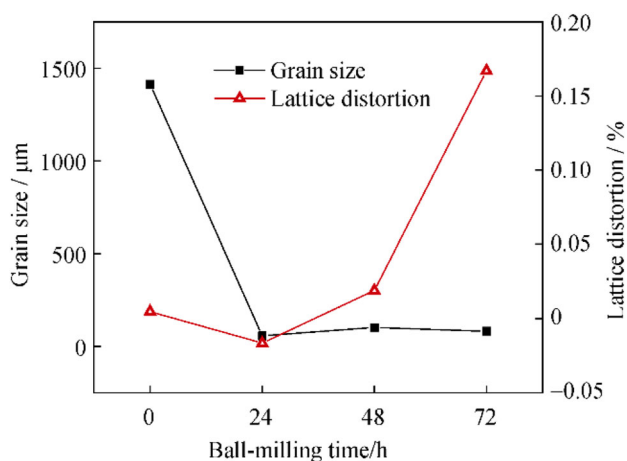
where β is the broadening of the diffraction peak measured by full width at half maximum (FWHM), θ is the diffraction angle, d_c is the diameter of crystalline size, and ζ is a constant. The constant ζ can be determined by the crystalline shape and the indices. It has a value of about 0.9.

The change of crystal spacing is Δd , which is considered as the supersaturated solid solution formed. In detail, the lattice distortion can be calculated by [26]:

$$\varepsilon = \frac{d - d_0}{d} = \frac{\Delta d}{d} \quad (9)$$

where d is interplanar spacing changes and ε is lattice distortion variables.

According to the principle above, the mean value of grain size and lattice distortion with different milling times has been calculated, and its relationship is shown in Fig. 4. As illustrated, before the ball milling ($t = 0$ h), the average grain size of the powder is much higher than 100 nm, calculated as 1413.23 nm. After ball milling for 24 h, the grain size drops sharply, hitting bottom at 57.1 nm, which is a nanometer crystal size. With the further extension of the ball-milling time, the grain size fluctuates in a small range, while the lattice distortion increases continuously.

**Fig. 4** Mean values of grain size and lattice distortion with different ball-milling time

After ball milling for 48 h, the grain size shows a tendency of slightly rebound, peaking at 101.73 nm. After ball milling for 72 h, the powder grain size attains to 81.21 nm.

It also shows that with the increase in milling time, the lattice distortion has ascended finally, indicating that the supersaturated solution occurs. By consulting the relevant data, the atomic radii of Sn, Fe, and B are 140, 126, and 90 pm, respectively. The atomic radius of Fe is close to that of Sn, but the atomic radius of B is much smaller than that of Sn. Consequently, B atoms can enter the interstitial space easily to form interstitial solid solution. That is to say, the B atoms can be accommodated in the lattice, causing the lattice distortions. After ball milling for 72 h, the lattice distortion increases to 0.1670%, which can be considered as a higher degree of alloying [27].

Combined with the degree of grain size and lattice distortion, it can be predicted that it is not significant to extend the ball-milling time longer. The reasons are shown as follows: (1) From the perspective of getting the fine crystal microstructure, the grains have been significantly refined after ball milling for 24 h, and the size shows a little change with the time increasing. Therefore, it indicates less effect on the microstructure with the ball-milling time increasing. (2) From the aspect of lattice distortion, although the degree of lattice distortion will continue to improve, combined with the previous ICP-AES element quantitative analysis, after ball milling for 72 h, the B content in the Sn-based alloy sample has reached 2.38%, which is almost equivalent to the addition of the B in the raw material. Continuing ball milling will cause the contamination of excessive SiO_2 impurities which come from the wastage of milling media (agate ball), and the pollution is detrimental to the alloy system. (3) From the view of practical application, with the increase in the ball-milling time, the energy consumption in the process will increase, and the production efficiency will reduce, which is disadvantageous to the industrialization.

3.1.5 Microstructural evolution

To explain the mechanism of samples' variations during mechanical alloying, the metallographic structure has been observed (Fig. 5). The metallograph shows that with the increase in the ball-milling time, the samples' particle size indicates the tendency of a rise after a decline, which is consistent with the law of mechanical alloying, i.e., the 'cold welding, crushing, cold welding' cyclic process.

To further study the effect of adding B and FeB on the microstructure and distribution of the matrix, SEM images are shown as follows (Fig. 6). Back-scattered electron SEM (BSE-SEM) images carry out a comparative illustration in contrast, in which the black area is B-rich phase, and the gray is the FeB phase. Furthermore, combining

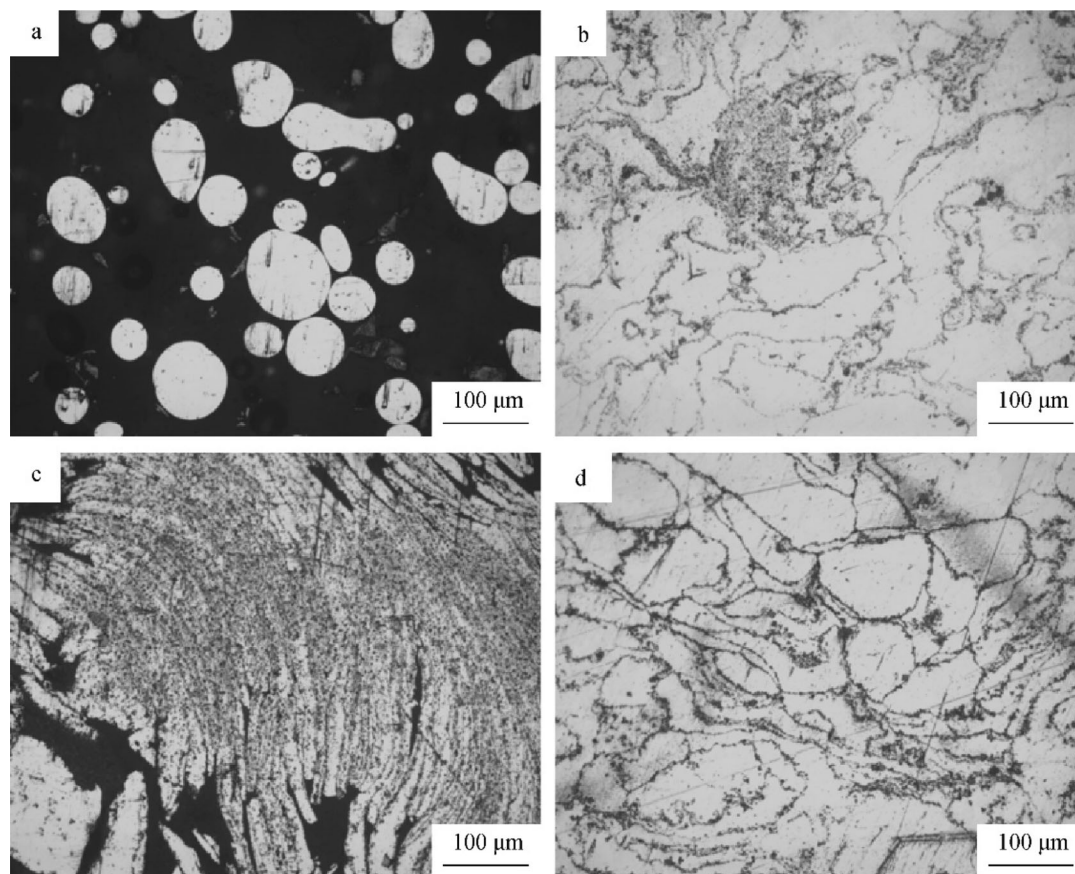


Fig. 5 OM images of Sn–Fe–B alloy with different ball-milling time: **a** blended powder $t = 0$ h, **b** $t = 24$ h, **c** $t = 48$ h, and **d** $t = 72$ h

with the elemental distribution map (Fig. 6), it can be concluded that the FeB and B have been distributing evenly with the ball-milling time increasing.

It can be seen that the gray phase (FeB) and black phase (B-rich phase) appear after ball milling. With the increase in milling time, the state of FeB and B in the matrix has been changed. At first, they distribute unevenly, and the agglomerations exist. However, after ball milling, they become fine and dispersive distribution.

3.1.6 Alloying microstructure

To further study the evolution law of microstructure with the increase in ball-milling time, the morphology of samples was characterized by SEM (Fig. 7). The different phases, i.e., the black area (α B-rich phase) and the gray area (β FeB phase), can be found in the microstructure after ball milling. Moreover, with the increase in milling time, the microstructural evolution occurs. (1) For $t = 24$ h, it shows an almost monopoly contrast with some obvious contrast of FeB and B. (2) For $t = 48$ h, it shows a contrast difference between FeB and B, besides some invisible transition zones. (3) For $t = 72$ h, it illustrates some obvious transition contrasts between dark and light {(FeB &

B)/matrix}, which can be considered as the alloying phase [28].

3.2 (Fe–B)-doped solder alloys

The trace (Fe–B)-doped SAC105 solder alloys were prepared by the Sn–Fe–B master alloys as synthesized before. The master alloys milled for 72 h were selected as the solder alloys' raw material because of the high alloying degree and the stable properties.

3.2.1 Microstructure of solder alloys

As shown in Fig. 8, the optical metallographic (OM) images demonstrate that the grain size has declined by the additions of 0.1(Fe–B), and the primary Sn accounts for a significant proportion of matrix volume. As illustrated in Fig. 8a, the composition segregation and coarse microstructure are present in the matrix. On the contrary, in the (Fe–B)-doped samples as illustrated in Fig. 8b, the primary Sn is finer than that in SAC105. It indicates that the (Fe–B) has a grain refinement effect because of the heterogeneous nucleation effect [29].

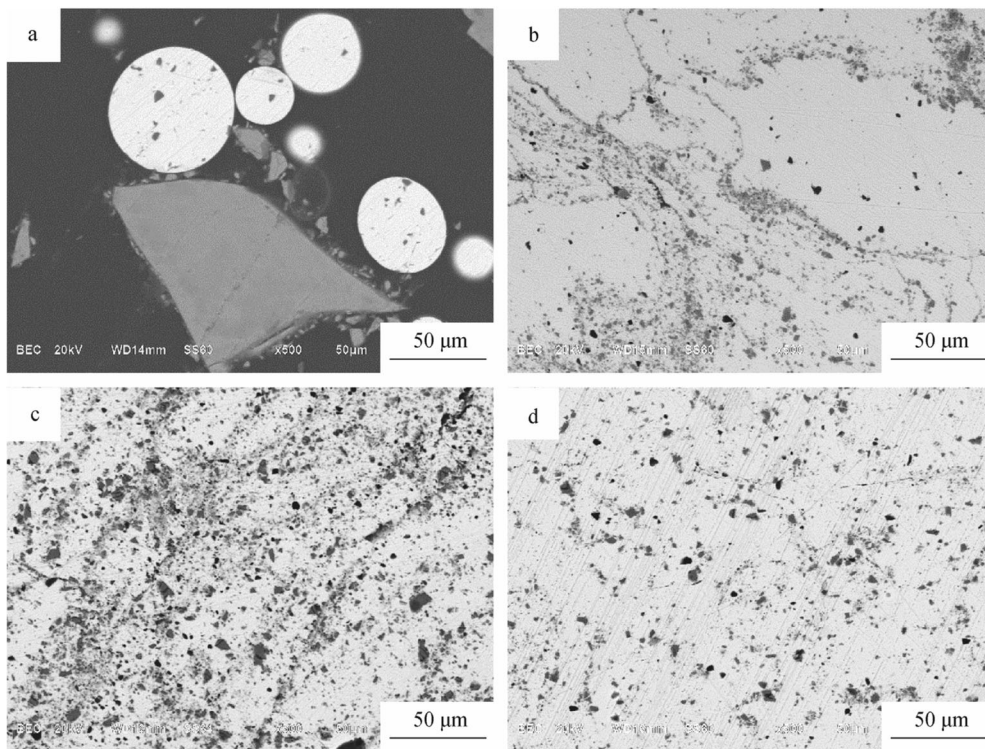


Fig. 6 BSE-SEM images of Sn–Fe–B alloys with different ball-milling time: **a** blended powder $t = 0$ h, **b** $t = 24$ h, **c** $t = 48$ h, and **d** $t = 72$ h

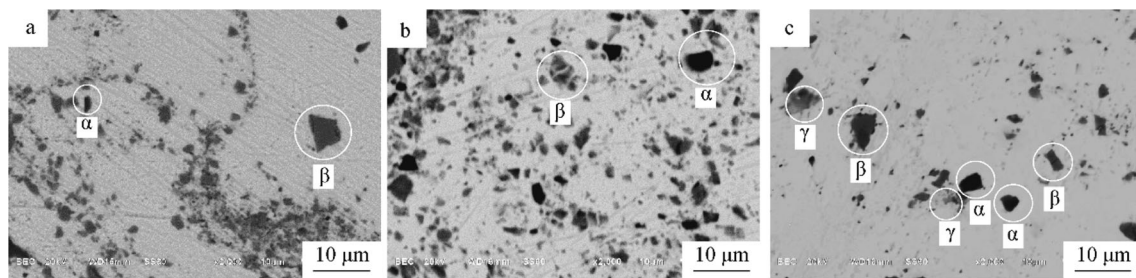


Fig. 7 BSE-SEM images of Sn–Fe–B alloy with different ball-milling time: **a** $t = 24$ h, **b** $t = 48$ h, and **c** $t = 72$ h (α is B-rich phase (black area); β is FeB phase (a gray area), and γ is alloying phase (between nanometregray and light))

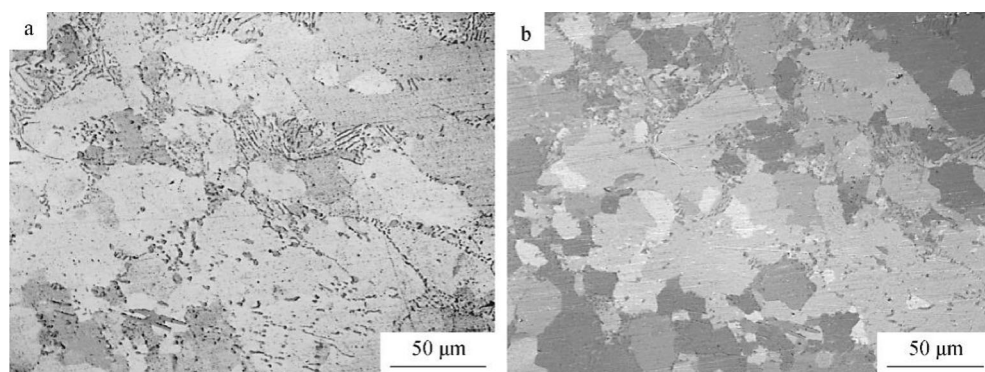


Fig. 8 OM images of **a** Sn–1.0Ag–0.5Cu, **b** Sn–1.0Ag–0.5Cu–0.1(Fe–B)

3.2.2 Melting behavior

The melting point of solder is one of the critical characteristics for the weldability and reliability of solders. Figure 9 shows DSC curves of samples (temperature measurement ranging from 0 to 350 °C). As illustrated in Fig. 9a, three different alloys have only one heat-absorbing peak. Moreover, the enlarge diagram around the peak of DSC curves is shown in Fig. 9b, and the initial melting temperature (onset) of the SAC105 is the biggest, peaking at 223.25 °C. However, the initial melting temperature of SAC105-0.05(Fe-B) and SAC105-0.1(Fe-B) is 218.8 and 217.7 °C, respectively. The melting starting temperature of the solder alloys decreases with the (Fe-B) content ascending. Among them, the liquid lines are around 230 °C, and melting processes are < 30 °C, which conforms to the requirements of the surface-mount technology (SMT) application [30]. It has been reported that the addition of Fe can reduce the melting point of the solder alloy [31]. In this study, when B is introduced with Fe as the carrier, this feature can be maintained. It is mainly attributed to the alloying reaction occurred in the solder alloys, which can also bring about interface instability and reduce the melting point of alloys. Most notably, the lower melting is conducive to the soldering process [32–34]. Thus, there is no need to change the temperature of the soldering procedure for the application of (Fe-B)-doped solders in this work.

3.2.3 Solder alloys hardness testing

The hardness values of solder alloys, before and after aging, are presented in Table 3 and Fig. 10. Furthermore, for the Fe-B alloys, the mass ratio of Fe and B is around 8:2. In order to decouple the influence of Fe and B, the SAC105–0.04Fe and SAC105–0.08Fe solders were also

Table 3 Hardness measurements of SAC105 and (Fe, B)-doped SAC105 solders (HLD)

Alloys	Microhardness indentation results					Ave.
	Trail 1	Trail 2	Trail 3	Trail 4	Trail 5	
SAC105	138	155	135	137	142	141.4
SAC105–0.04Fe	148	158	148	154	160	153.6
SAC105–0.04Fe–0.01B	185	151	174	177	166	170.6
SAC105–0.08Fe	176	183	175	179	174	177.4
SAC105–0.08Fe–0.02B	189	183	195	186	200	190.6

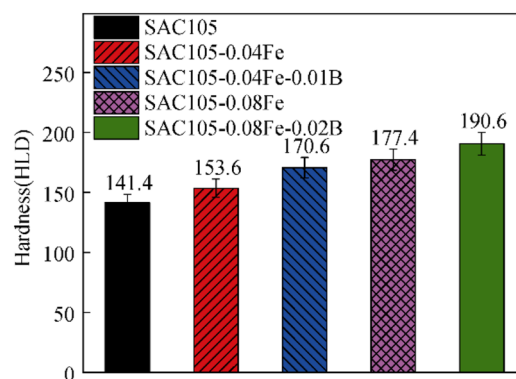


Fig. 10 Average hardness results of different solders according to Table 3

prepared and assessed. The measured results indicate that the (Fe-B)-doped SAC105 alloys have higher hardness than ordinary SAC105 solder. In detail, compared to the benchmark SAC105, the hardness of SAC105–0.05(Fe-B) and SAC105-0.1(Fe-B) solder alloys prepared by this

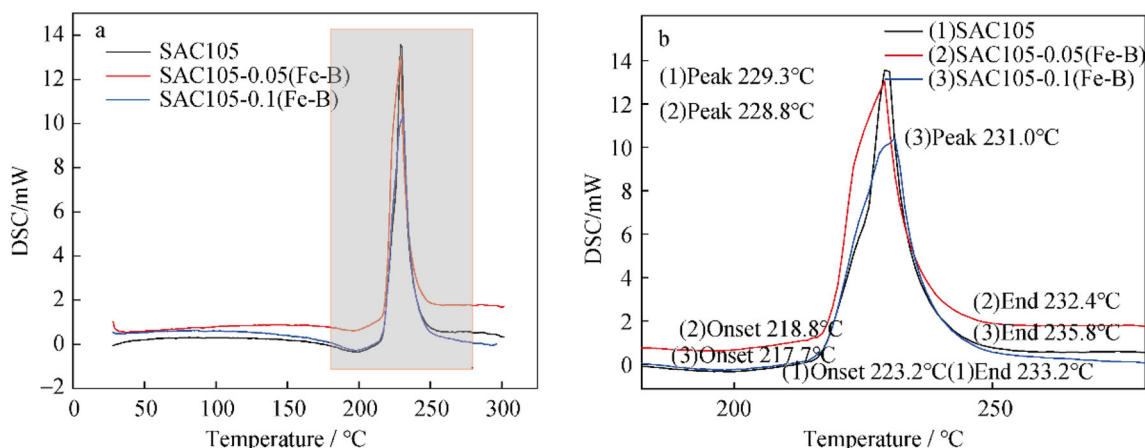


Fig. 9 Melting characteristics of different solder alloys: **a** DSC curves and **b** enlarge diagram around peak of DSC curves

method has improved by 20.65% and 34.79%, respectively. This hardness variation can reflect the microstructural changes observed in Fig. 8. Mechanisms of hardness enhancement can be attributed to the following reasons: (1) The (Fe–B)-doped solder alloys have finer microstructure Ag_3Sn and Cu_6Sn_5 particles, thus promoting the precipitation hardening effect. (2) The finely dispersed compounds have a dispersion enhancing which brings about the hardness improvement in the solder alloys [35]. (3) The pinning effect and the linear dislocations ascend, which brings out the increase in dislocation density, increasing the barrier boundaries and limiting the particle motion [36]. (4) The dispersed distribution of (Fe–B) in the solder alloys hinders the growth of crystal grains [6]. In addition, it can be obviously seen that the hardness of (Fe–B)-containing solders is significantly higher than that of the mono-Fe-containing solders. Thus, Fe can be determined as the competent carrier to introduce B into the solders. Under the combined action of Fe and B, the hardness of solder alloy has been significantly improved.

4 Conclusion

In this work, the immiscible component boron (B) was successfully introduced into the Sn–1.0Ag–0.5Cu solders by using the Sn–Fe–B master alloy. During the mechanical alloying process, the particle size of powder samples illustrates the cyclic process of ‘cold welding, crushing, and cold welding.’ After milling for 72 h, the content of B reaches the initial addition amount of 2.38 wt%, and the high alloying degree with the lattice distortion of 0.167% has been achieved.

Moreover, with the addition of (Fe–B), a lower melting point has attained, meeting the requirement of soldering process. Meanwhile, a grain refinement effect has been obtained. According to the hardness test, the properties of solders containing Fe and B are superior to that of mono-Fe addition. Combining with the thermodynamic calculation, Fe can be determined as a competent carrier to introduce B into the solders. Under the coupling effect of Fe and B, the mechanical property of Sn–1.0Ag–0.5Cu solder alloys has been improved significantly.

Acknowledgements This study was financially supported by the National Key R&D Program of China (No. 2017YFB0305703).

References

- [1] Abtey M, Selvaduray G. Lead-free Solders in Microelectronics. *Mater Sci Eng R*. 2000;27(5):95.
- [2] Mustafa M, Suhling JC, Lall P. Experimental determination of fatigue behavior of lead free solder joints in microelectronic packaging subjected to isothermal aging. *Microelectron Reliab*. 2016;56:136.
- [3] Zou CD, Gao YL, Yang B, Xia XZ, Zhai QJ, Andersson C, Liu J. Nanoparticles of the lead-free solder alloy Sn–3.0Ag–0.5Cu with large melting temperature depression. *J Electron Mater*. 2009;38(2):351.
- [4] Wang Y, Zhao XC, Liu Y, Wang Y, Li DM. Microstructure, wetting property of Sn–Ag–Cu–Bi– x Ce solder and IMC growth at solder/Cu interface during thermal cycling. *Rare Met*. 2015. <https://doi.org/10.1007/s12598-015-0526-1>.
- [5] Sui YW, Sun R, Qi JQ, He YZ, Wei FX, Meng QK, Sun Z. Morphologies and evolution of intermetallic compounds formed between Sn1.0Ag0.7Cu composite solder and Cu substrate. *Rare Met*. 2017. <https://doi.org/10.1007/s12598-017-0968-8>.
- [6] Qu JF, Xu J, Hu Q, Zhang FW, Zhang SM. Modification of Sn–1.0Ag–0.5Cu solder using nickel and boron. *Rare Met*. 2015; 34(11):783.
- [7] Sun L, Chen M, Zhang L, Yang F. Microstructures evolution and properties of Sn–Ag–Cu solder joints. *Acta Metall Sin*. 2017;53(5):615.
- [8] Mahdaviifard MH, Sabri MFMM, Shnawah DA, Said SM, Badruddin IA, Rozali S. The effect of iron and bismuth addition on the microstructural, mechanical, and thermal properties of Sn–1Ag–0.5Cu solder alloy. *Microelectron Reliab*. 2015; 55(9–10):1886.
- [9] Choi H, Lee TK, Kim Y, Kwon H, Tseng CF, Duh JG, Choe H. Improved strength of boron-doped Sn–1.0Ag–0.5Cu solder joints under aging conditions. *Intermetallics*. 2012;20(1):155.
- [10] Ye L, Lai ZH, Liu J, Thölén A. Microstructure investigation of Sn–0.5Cu–3.5Ag and Sn–3.5Ag–0.5Cu–0.5B lead-free solders. *Solder Surf Mt Technol*. 2001;13(3):16.
- [11] Wang RD, Zhang SM, Hu Q, Zhang FW. Effect of boron on microstructure and properties of Sn–1.0Ag–0.5Cu low-silver lead-free solder. *Mater Sci Forum*. 2017;898:908.
- [12] Suryanarayana C. Mechanical alloying and milling. *Prog Mater Sci*. 2001;46(1):1.
- [13] Weeber AW, Bakker H. Amorphization by ball milling. A review. *Phys B Phys Condens Matter*. 1988;153(1):93.
- [14] Wu ZF, Wu J, Zhang L, Liu C, Wu R. Solid solubility extension of copper-tin immiscible system during mechanical alloying. *Materialwiss Werkstofftech*. 2018;49(1):54.
- [15] Shingu PH, Ishihara KN. Non-equilibrium materials by mechanical alloying (overview). *Mater Trans JIM*. 1995;36(2): 96.
- [16] Miedema AR, De Châtel PF, De Boer FR. Cohesion in alloys—fundamentals of a semi-empirical model. *Physica B + C*. 1980;100(1):1.
- [17] De Boer FR, Mattens WCM, Boom R, Miedema AR, Niessen AK, De Boer FR, Mattens WCM, Boom R. Cohesion in Metals[J]. 1988.
- [18] Dębski A, Dębski R, Gasior W. New features of Entall database: comparison of experimental and model formation enthalpies. *Arch Metall Mater*. 2014;59(4):1337.
- [19] Zhang RF, Rajan K. Statistically based assessment of formation enthalpy for intermetallic compounds. *Chem Phys Lett*. 2014; 612:177.
- [20] Chen ZH, Chen D. Mechanical alloying and solid–liquid reaction ball milling. Beijing: Chemical Industry Press; 2006. 34.
- [21] Ma E, Sheng HW, He JH, Schilling PJ. Solid-state alloying in nanostructured binary systems with positive heat of mixing. *Mater Sci Eng A*. 2000;286(1):48.
- [22] Yavari AR, Desré PJ. Thermodynamics and kinetics of amorphisation during mechanical alloying[C]//Materials Science Forum. Trans Tech Publications. 1992; 88: 43.
- [23] Yamane T, Okubo H, Oki N, Hisayuki K, Konishi M, Minamino Y, Koizumi Y, Kiritani M, Komatsu M, Kin SJ. Impact

- consolidation of mixed copper and carbon powders mechanically alloyed. *J Jpn Soc Powder Powder Metall.* 2009;48(1):9.
- [24] Wei ZQ, Xia TD, Wang J, Wu ZG, Yan PX. Lattice expansion of Ni nanopowders. *Acta Phys Sin.* 2007;56(2):1004.
- [25] Lü L, Lai MO. *Mechanical Alloying*. Boston: Springer; 1998. 166.
- [26] Li L, Wang W, Hu L, Ying R, Wei B. Lattice properties of supersaturated Ni–Sn solid solutions. *Mater Lett.* 2015;160:72.
- [27] Yao ZH. Research on properties and microstructure of 12Cr-ODS Fe-based superalloy fabricated by mechanical alloying. Wuhan: Huazhong University of Science & Technology; 2011. 32.
- [28] Nouri A, Hodgson PD, Wen C. Effect of ball-milling time on the structural characteristics of biomedical porous Ti–Sn–Nb alloy. *Mater Sci Eng C.* 2011;31(5):921.
- [29] Liu X, Wu Y, Bian X. The nucleation sites of primary Si in Al–Si alloys after addition of boron and phosphorus. *J Alloys Compd.* 2005;391(1):90.
- [30] Zhuang HS. New development of lead-free solders. *Electron Process Technol.* 2001;22(5):192.
- [31] Fallahi H, Nurulakmal MS, Arezodar AF, Abdullah J. Effect of iron and indium on IMC formation and mechanical properties of lead-free solder. *Mater Sci Eng A.* 2012;553:22.
- [32] Roshanghias A, Vrestal J, Yakymovych A, Richter KW, Ipsier H. Sn–Ag–Cu nanosolders: melting behavior and phase diagram prediction in the Sn-rich corner of the ternary system. *CALPHAD: Comput Coupling Phase Diagrams Thermochem.* 2015; 49:101.
- [33] Liu Q, Orme M. High precision solder droplet printing technology and the state-of-the-art. *J Mater Process Technol.* 2001; 115(3):271.
- [34] Jung DH, Sharma A, Jung JP. Influence of dual ceramic nanomaterials on the solderability and interfacial reactions between lead-free Sn–Ag–Cu and a Cu conductor. *J Alloys Compd.* 2018; 743:300.
- [35] Ali B, Sabri MFM, Jauhari I, Sukiman NL. Impact toughness, hardness and shear strength of Fe and Bi added Sn–1Ag–0.5Cu lead-free solders. *Microelectron Reliab.* 2016;63:224.
- [36] Wu CML, Yu DQ, Law CMT, Wang L. Properties of lead-free solder alloys with rare earth element additions. *Mater Sci Eng R: Rep.* 2004;44(1):1.